Pulsed- and continuous-wave difference-frequency generation in AlGaAs Bragg reflection waveguides

J. B. Han, D. P. Kang, P. Abolghasem, B. J. Bijlani, and A. S. Helmy*

The Edward S. Rogers Sr. Department of Electrical and Computer Engineering, University of Toronto, 10 King's College Road, Toronto, Ontario M5S 3G4, Canada
**Corresponding author: a.helmy@utoronto.ca*

Received July 22, 2010; accepted September 24, 2010;
posted September 28, 2010 (Doc. ID 132029); published November 3, 2010

Pulsed- and continuous-wave type-I and type-II difference-frequency generations (DFGs) in monolithic AlGaAs Bragg reflection waveguides were comparatively investigated. Phase matching bandwidth of exceeding 40 nm was observed in all the processes. Highest difference-frequency (DF) power of 2.45 nW was obtained in continuous-wave type-II interaction with the average external pump and signal powers of 62.9 and 2.9 mW, respectively. The corresponding nonlinear conversion efficiency is about $1.3\times10^{-3}\%$ W^{-1} for a sample with a length of 1.5 mm. Using split-step Fourier method, the impacts of third-order nonlinearities including two-photon absorption and self-phase modulation on the efficiency of the DFG are numerically investigated. Furthermore, the adverse effects of group velocity mismatch and group velocity dispersion of the interacting frequencies on the efficiency of the pulsed nonlinear process are theoretically studied. Simulations indicate that the dominant factors in limiting the efficiency of the pulsed interaction are group velocity mismatch between pump and DF signal and two-photon absorption of the interacting waves.

OCIS codes: 190.2620, 160.4330, 230.1480, 130.3120.

1. INTRODUCTION

The generation of tunable coherent infrared radiation is significant for many applications such as gas sensing [1,2], time-resolved spectroscopy [3], biological and medical diagnostics [4], and optical coherence tomography [5]. Difference-frequency generation (DFG) is an attractive technique for the generation of widely tunable coherent infrared radiation where no appropriate laser medium exists [6–8]. Today's most versatile sources for mid-infrared spectroscopy are relatively bulky optical parametric oscillators (OPOs) based on crystals such as $LiNbO_3$ and KTP. Such crystals exhibit large material absorption above 5 μm [9] which limits their operating range for infrared generation. AlGaAs is an appealing alternative to bulk crystals thanks to its broader transparency window (0.9–17 μm), high second-order nonlinearity, well-established fabrication technology, and the potential for monolithic integration of active and passive elements. Nevertheless, the lack of natural birefringence in AlGaAs renders phase-matching (PM) $\chi^{(2)}$ processes challenging. To date, several techniques have been successfully reported for PM DFG process in AlGaAs such as form-birefringence phase-matching (BPM) [10,11] and quasi-phase-matching (QPM) [12,13]. Among these, BPM has been shown to be the most efficient technique. However, the necessity of incorporating AlO_x layers with high absorption above 7.5 μm along with the absorption of GaAs below 870 nm limits the operating window of BPM devices for infrared generation [6].

Another promising PM technique makes use of Bragg reflection waveguides (BRWs). It utilizes the strong modal dispersion properties of photonic bandgap structures [14,15]. Unlike BPM waveguides which involve invoking AlO_x elements and domain-reversal QPM waveguides which involve demanding overgrowth technology, BRWs benefit from structural simplicity which makes their fabrication feasible using simple epitaxial growth techniques such as metal-organic chemical-vapor deposition. This in turn enables the realization of novel monolithically integrated parametric devices, where active elements such as diode laser pumps, photodetectors, and passive elements such as nonlinear frequency mixing waveguides can be integrated on the same platform without the necessity of exploiting complex hybrid fabrication techniques.

For $\chi^{(2)}$ devices that operate with ultrashort pulses, group velocity mismatch (GVM) and group velocity dispersion (GVD), as well as the effects of third-order optical nonlinearities $\chi^{(3)}$ such as two-photon absorption (TPA) and self-phase modulation (SPM) should be taken into consideration in the design phase. This is especially true when the interacting wavelength lies close to the material resonances of the nonlinear medium where dispersion is significant. The GVM leads to a temporal pulse walk-off between the harmonics, while the GVD results in a broadening of the pulses. TPA and SPM are power dependent, and their effects on the $\chi^{(2)}$ process become significant when the operating peak power is high [16,17]. The effects of dispersion and $\chi^{(3)}$ on femtosecond second-harmonic generation of BRWs have been previously reported in [17]. However their effects on DFG have not been reported yet. In this paper, the impact of $\chi^{(3)}$ including TPA and SPM and dispersion including GVM and GVD on DFG will be comparatively investigated experimentally and theoretically in both pulsed- and continuous-wave (cw) regimes.

The organization of this paper is as follows. Section 2 describes the waveguides and the setup that were used during the experiments; Subsection 2.A demonstrates the pulsed pumped type-I and type-II DFG processes; Subsection 2.B presents the cw DFG results. Section 3 provides an overview of the theoretical frame work, while Section 4 discusses the simulation results, where detailed analysis of the effects of $\chi^{(3)}$ nonlinearity and dispersion on DFG is presented. Section 5 discusses the limitations of BRWs and some possible solutions. Conclusions are summarized in Section 6.

2. CHARACTERIZATION RESULTS

Detailed description of the epitaxial structure has been previously reported in [18]. The device characterized here was a ridge waveguide with a ridge width of 4.4 μm and an etch depth of 3.6 μm. The length of the sample was 1.5 mm. The propagation losses of signal and difference frequency (DF) around 1550 nm were measured as 2.0 and 2.2 cm^{-1} for transverse-electric (TE) and transverse-magnetic (TM) polarizations, respectively. The propagation loss of the pump could not be measured directly owing to the complexities involved in preferential coupling into the Bragg mode, where total internal reflection modes also co-exist.

Device characterization was carried out in an end-fire coupling setup [19]. For a pulsed pumped DFG process, a 2 ps mode-locked Ti:Sapphire laser operating around 775 nm with a repetition rate of 76 MHz was used as the pump source, while for a cw DFG process, Ti:Sapphire laser was switched to cw mode. The signal was taken from a cw *C*-band tunable laser amplified by an erbium-doped fiber amplifier (EDFA). A tunable fiber grating filter was cascaded with the EDFA to suppress the amplified spontaneous emission of the EDFA below the level of the DF signal. The tunability of the signal wavelength was limited to the 1532–1572 nm range. The range was imposed by the *C*-band operation of the EDFA and the fiber grating filter. Absolute measurement of the DF power requires separation of signal and idler waves at the waveguide output and the use of a phase-sensitive detection setup. However, due to the proximity of signal and DF wavelengths, the beams could not be separated spatially either by using a dispersion prism or by employing narrow-line spectral filters. Here, the DF power was estimated by carefully calibrating an optical spectrum analyzer (OSA) and integrating the area underneath of the DF spectra recorded by the OSA. Both type-I (TM-polarized pump and TE-polarized signal generates TE-polarized DF) and type-II (TE-polarized pump and signal generates TM-polarized DF) DFGs pumped by pulsed wave and cw were examined in this experiment.

A. Pulsed-Wave-Pumped DFG

Figure 1 shows the DF power (P_{DF}) plotted as a function of the pulsed pump wavelength for both type-I (hollow circles) and type-II (filled circles) interactions with λ_s set as 1545.9 nm. The dashed and solid lines are the corresponding Lorentzian fits to the data. In obtaining the tuning curve in Fig. 1, the external average pump (P_p) and signal (P_s) powers, measured before the front facet of the sample, were fixed to 62.9 and 2.9 mW, respectively. From the experiments, peak DF powers, estimated right after the exit facet of the waveguide, were obtained to be 0.22 and 0.95 nW for the phase-matched type-I and type-II processes, respectively. The pump acceptance bandwidths ($\Delta\lambda_p$) of the type-I and type-II DFG processes were found to be 0.66 and 0.48 nm, respectively.

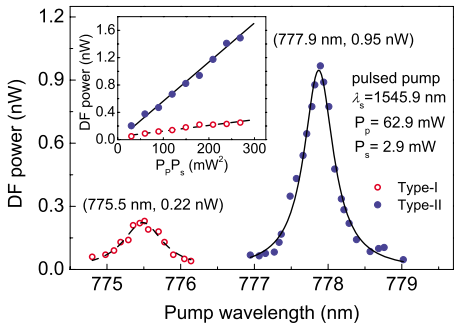

Fig. 1. (Color online) Variation of the DF power as a function of pulsed pump wavelength for λ_s=1545.9 nm. Hollow and filled circles are the experimental data for type-I and type-II interactions, respectively. The dashed and solid lines are Lorentzian fits to the corresponding data. (Inset) Dependence of P_{DF} on P_pP_s for type-I (hollow circles) and type-II (filled circles) interactions.

In the DFG process, P_{DF} is proportional to the product of pump and signal powers (P_pP_s). We verified this relation for a fixed pump power of 62.9 mW and a signal sweeping power range of 0.48–4.8 mW. The results are shown in the inset of Fig. 1; the hollow and filled circles are the data obtained from type-I and type-II processes, respectively, while the lines are linear fits to the data which provide an estimation of the DFG conversion efficiency η, which is defined as $\eta=P_{DF}/(P_pP_s)$. For the characterized device, η was found to be $\approx 1.2\times10^{-4}\%$ W^{-1} and $5.2\times10^{-4}\%$ W^{-1} for the type-I and type-II processes, respectively. The corresponding normalized conversion efficiencies to the device length (L) were $5.4\times10^{-3}\%$ W^{-1} cm^{-2} and $2.3\times10^{-2}\%$ W^{-1} cm^{-2}, respectively. It should be noted that the DFG efficiency reported here is the external value. The internal efficiency, which requires the estimation of the internal powers inside the device, is considerably larger than the external one. The internal pump power could not be determined due to difficulties in extracting the linear coupling factor defined as the spatial overlap between the incident pump beam and the excited pump Bragg mode. Simulations indicate that this coupling efficiency is likely to be a few percent with an upper-limit value of 5%, which implies that a low pump power level is likely to be responsible for the output powers measured.

A typical spectrum taken at the waveguide output is shown in Fig. 2. Figures 2(a) and 2(b) are spectra for type-I and type-II processes, respectively. The pump central wavelength (λ_p) was set at degeneracy with a signal wavelength (λ_s) at 1545.9 nm. From the spectra, the peak powers of DF are about −67.0 and −62.5 dB smaller than those of the signals for type-I and type-II processes, respectively. The spectra in Fig. 2 denote an additional spectral feature at $2\lambda_p$, which is due to the second-order diffraction of the pump from the grating of the OSA. This was confirmed by the fact that the spectral feature at $2\lambda_p$

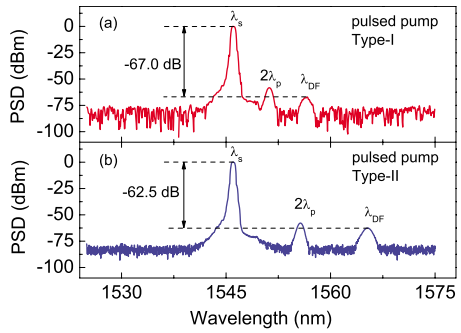

Fig. 2. (Color online) Normalized power spectral density (PSD) of the signal at 1545.9 nm (λ_s) and the converted DF (λ_{DF}). (a) Type-I interaction, (b) type-II interaction. The central peak with the wavelength of $2\lambda_p$ is the second-order diffraction of the pump from the OSA internal grating.

remained unchanged, while the DF wavelength (λ_{DF}) shifted in the opposite direction to the signal during tuning.

A key parameter for a DFG device is the PM bandwidth, $\Delta\lambda_{DFG}$, which determines the useful spectral range within which frequency conversion is efficient. To determine $\Delta\lambda_{DFG}$, the pump was set at the degeneracy, while the generated DF power was monitored and recorded versus signal wavelength in the range of 1532–1572 nm. The results are illustrated in Fig. 3, where the hollow and filled circles give the measured data for type-I and type-II interactions, respectively. The variation in the data was caused by the cavity resonance effect. Broadband PM was obtained around 1550 nm with $\Delta\lambda_{DFG}$ exceeding 40 nm for both type-I and type-II interactions, and no sign of bandwidth limitation was observed. Complete measurement of $\Delta\lambda_{DFG}$ could not be carried out due to the wavelength limitation of the *C*-band tunable signal laser and the fiber grating filter.

Figure 4 shows the type-I and type-II DFG tuning curves, which were obtained by detuning the pump wavelength from degeneracy while tracking the wavelengths of signal and DF for maximal DF power. It was observed that a fine detuning of the pump wavelength results in a broad span of wavelength between signal and DF wavelengths for both type-I and type-II interactions. Further detuning of the pump from degeneracy was expected to offer broader separation between signal and DF. This could not be confirmed experimentally due to the aforementioned constraints in tuning the signal wavelength.

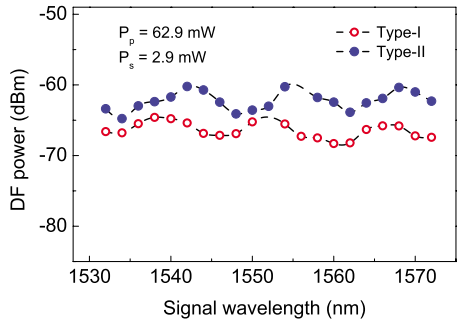

Fig. 3. (Color online) DF power as a function of signal wavelength with the pump wavelength set at the degeneracy. The hollow and filled circles are the measured data for type-I and type-II interactions, respectively.

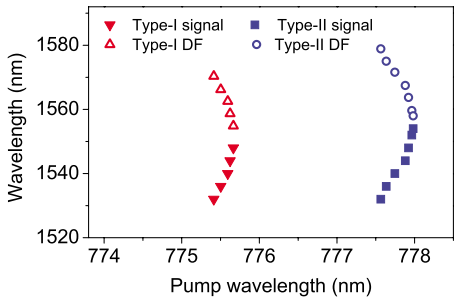

Fig. 4. (Color online) Signal and DF wavelengths as functions of pump wavelength for type-I and type-II interactions.

B. Continuous-Wave-Pumped DFG

In this subsection, cw DFG was characterized in the identical waveguide; all the experimental parameters except the pump pulse duration were set identical to those in Subsection 2.A. Fig. 5 shows the DF power plotted as a function of the cw pump wavelength for both type-I (hollow circles) and type-II (solid circles) interactions with λ_s set as 1545.9 nm. The dashed and solid lines are Lorentzian fits to the data. The experimental procedure and the average pump and signal powers are the same as those used in Subsection 2.A. Maximum DF powers of 0.31 and 2.45 nW were obtained for the phase-matched type-I and type-II processes, respectively. $\Delta\lambda_p$'s of the DFG processes were found to be 0.26 and 0.17 nm, respectively. The corresponding P_{DF} power versus P_pP_s was given in the inset of Fig. 5; the hollow and filled circles are experimental data, while the dashed and solid lines are linear fits. η was found to be $\approx 1.7\times10^{-4}\%$ W^{-1} and $1.3\times10^{-3}\%$ W^{-1} for type-I and type-II processes, respectively. The corresponding normalized conversion efficiencies to the device length were $7.6\times10^{-3}\%$ W^{-1} cm^{-2} and $5.8\times10^{-2}\%$ W^{-1} cm^{-2}, respectively.

The typical spectra taken at the waveguide output for (a) type-I and (b) type-II interactions are shown in Fig. 6. The pump central wavelengths were set at degeneracy with a signal at 1545.9 nm. From the spectra, the peak powers of DF are about −65.4 and −57.1 dB smaller than those of the signals, respectively. Figure 7 is DFG power versus signal wavelength in the range of 1532–1572 nm where the pump wavelength was set at the degeneracy. $\Delta\lambda_{DFG}$'s of both type-I and type-II processes were obtained to be larger than 40 nm.

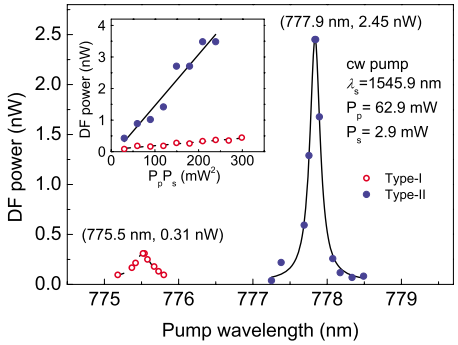

Fig. 5. (Color online) Variation of the DF power as a function of cw pump wavelength for λ_s=1545.9 nm. Hollow and filled circles are the experimental data for type-I and type-II interactions, respectively. The dashed and solid lines are Lorentzian fits to the corresponding data. (Inset) Dependence of P_{DF} on P_pP_s for type-I (hollow circles) and type- II (filled circles) interactions.

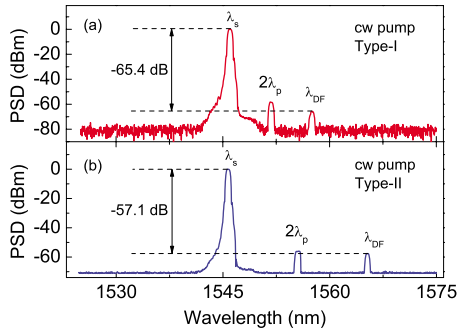

Fig. 6. (Color online) Normalized PSD of the signal at 1545.9 nm (λ_s) and the converted DF (λ_{DF}). (a) Type-I interaction, (b) type-II interaction. The central peak with the wavelength of $2\lambda_p$ is the second-order diffraction of the pump from the OSA internal grating.

A summary of the external average pump and signal powers, generated DF powers, pump acceptance bandwidth, signal tuning bandwidth, conversion efficiency, and normalized conversion efficiency of pulsed-wave- and cw-pumped type-I and type-II DFG interactions is given in Table 1. The cw-pumped type-II interaction is evident to be the most efficient one. In the following two sections, numerical analysis based on the coupled-mode equations was done to analyze these two interaction processes, and the main limitations of the pulsed pumped DFG were demonstrated.

3. THEORETICAL FRAMEWORK

In this section, the theoretical framework that describes the DFG process is detailed. This provides the platform where the effects of $\chi^{(3)}$ and mode dispersions on the outcome DF are examined. The DFG process involves three waves interactions which include a pump at wavelength λ_p, a signal at λ_s, and a DF at λ_{DF}. We assume a collinear interaction in the waveguide along the z-axis and express the electric fields of the harmonics as

$$E_i(x,y,z,t) = A_i(z)E_i(x,y)\exp[-j(\beta_i z - \omega_i t)], \tag{1}$$

where $i \in \{p,s,\mathrm{DF}\}$, $A_i(z)$ is the slowly varying amplitude, ω_i is the angular frequency, $E_i(x,y)$ is the normalized spatial field profile, and β_i is the propagation constant, $\beta_i = 2\pi n_i/\lambda_i$, where n_i is the effective mode index. The evolution of slowly varying amplitudes $A_i(z)$ along the propagation direction can be described by the coupled-mode equations as [20,21]

$$\frac{dA_p}{dz} = -j\kappa_p \nu A_s A_{\mathrm{DF}} \exp[j\Delta\beta z] - \frac{1}{v_{g,p}}\frac{dA_p}{dt} + \frac{j\beta_{2,p}}{2}\frac{dA_p^2}{dt^2} - \frac{\alpha_{0,p}}{2}A_p - \left[\frac{\alpha_{2,p}}{2} - j\frac{2\pi n_{2,p}}{\lambda_p}\right]\frac{|A_p|^2}{A_{\mathrm{eff},p}^{(3)}}A_p, \tag{2}$$

$$\frac{dA_s}{dz} = -j\kappa_s \nu^* A_p^* A_{\mathrm{DF}} \exp[-j\Delta\beta z] - \frac{1}{v_{g,s}}\frac{dA_s}{dt} + \frac{j\beta_{2,s}}{2}\frac{dA_s^2}{dt^2} - \frac{\alpha_{0,s}}{2}A_s - \left[\frac{\alpha_{2,s}}{2} - j\frac{2\pi n_{2,s}}{\lambda_s}\right]\frac{|A_s|^2}{A_{\mathrm{eff},s}^{(3)}}A_s, \tag{3}$$

$$\frac{dA_{\mathrm{DF}}}{dz} = -j\kappa_{\mathrm{DF}} \nu^* A_p^* A_s \exp[-j\Delta\beta z] - \frac{1}{v_{g,\mathrm{DF}}}\frac{dA_{\mathrm{DF}}}{dt} + \frac{j\beta_{2,\mathrm{DF}}}{2}\frac{dA_{\mathrm{DF}}^2}{dt^2} - \frac{\alpha_{0,\mathrm{DF}}}{2}A_{\mathrm{DF}} - \left[\frac{\alpha_{2,\mathrm{DF}}}{2} - j\frac{2\pi n_{2,\mathrm{DF}}}{\lambda_{\mathrm{DF}}}\right]\frac{|A_{\mathrm{DF}}|^2}{A_{\mathrm{eff,DF}}^{(3)}}A_{\mathrm{DF}}, \tag{4}$$

where $\Delta\beta = \beta_p - \beta_s - \beta_{\mathrm{DF}}$ is the wave number mismatch; $v_{g,i}$ is the group velocity; $\beta_{2,i}$ is the GVD parameter; ν is the spatial nonlinear overlap factor; $\alpha_{0,i}$ is the linear loss coefficient; $\alpha_{2,i}$ and $n_{2,i}$ are effective TPA and SPM coefficients of the structure, respectively; and $A_{\mathrm{eff},i}^{(3)}$ is the third-order effective area [17]. The pulse envelope is normalized such that the harmonic power P_i can be expressed as $P_i = |A_i|^2$. In Eqs. (2)–(4), the coupling coefficient κ_i is given by

$$\kappa_i = \left(\frac{8\pi^2 d_{\mathrm{eff}}^2}{n_p n_s n_{\mathrm{DF}} c\,\epsilon_0 \lambda_i^2}\right)^{1/2}, \tag{5}$$

where c is vacuum speed of light and d_{eff} is the effective second- order nonlinear coefficient [17].

In parametric processes involving ultrashort optical pulses, first- and second-order modal dispersions can considerably influence the efficiency of the nonlinear interaction. The first-order dispersion is generally quantified by GVM, which accounts for the temporal pulse walk-off between the harmonics. Due to the mismatch between the group velocities among the interacting frequencies, the harmonics with an initial temporal overlap progressively undergo temporal separation. For DFG, by definition, GVM between the DF and p is $\mathrm{GVM}_{\mathrm{DF},p} = 1/v_{g,\mathrm{DF}} - 1/v_{g,p}$. Second-order modal dispersion properties can also have degrading effects on the efficiency of the nonlinear interaction. Of particular importance is the GVD, which manifests itself in the pulse broadening, hence reducing the pulse peak power [17]. The presence of $\chi^{(3)}$, including TPA and SPM, under high pump power condition can further affect the efficiency of DFG. TPA causes an increase in the absorption coefficient that is proportional to the intensity of the optical field, while SPM leads to nonlinear phase shifting and spectral broadening of optical pulses, which is also dependent on the power intensity.

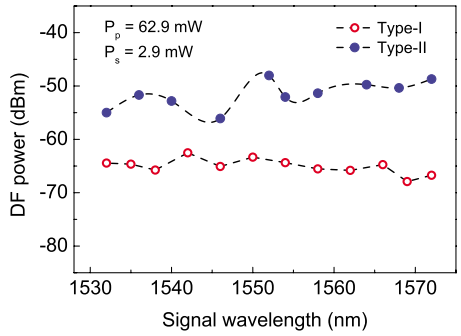

Fig. 7. (Color online) DF power as a function of signal wavelength with the pump wavelength set at the degeneracy. The hollow circles and filled circles are the measured data for type-I and type-II cw interactions, respectively.

Table 1. Comparison of Type-I and Type-II DFG Interactions with Pulsed-Wave and cw Pumps

DFG Process	P_p (mW)	P_s (mW)	P_{DF} (nW)	$\Delta\lambda_p$ (nm)	$\Delta\lambda_{DFG}$ (nm)	$P_{DF}/(P_pP_s)$ (% W^{-1})	$P_{DF}/(P_pP_sL^2)$ (% W^{-1} cm^2)
Type-I-Pulsed	62.9	2.9	0.22	0.66	>40	1.2×10^{-4}	5.4×10^{-3}
Type-II-Pulsed	62.9	2.9	0.95	0.48	>40	5.2×10^{-4}	2.3×10^{-2}
Type-I-cw	62.9	2.9	0.31	0.26	>40	1.7×10^{-4}	7.6×10^{-3}
Type-II-cw	62.9	2.9	2.45	0.17	>40	1.3×10^{-3}	5.8×10^{-2}

4. SIMULATION RESULTS

The aforementioned theory is now used to examine the effects of numerous parameters on the efficiency of DFG, and then the results were used to analyze the experimental DFG processes. For numerically solving the coupled-mode equations (2)–(4), we employed the split-step Fourier method [21], where dispersion parameters as well as $\chi^{(3)}$ effects were included. Simulations were run such that the peak power of one wave remained fixed at $t=0$, while the other waves were allowed to change. Details of the waveguide geometry were previously reported [18]. Here, we use a type-II DFG process for simulation where TE-polarized pump and signal generated TM-polarized DF. A summary of all the simulation parameters is given in Table 2. The values of $\alpha_{2,i}$ and $n_{2,i}$ were chosen from the maximum value of those in the layers of the structure which were evaluated from [22–25].

Figure 8 shows the variation of the DF power as a function of the device length with a 2 ps pulsed pump and a cw signal. In the simulation, the average internal pump power P_p was set as 3.1 mW which was taken from the upper-limit coupling of the external power used in the experiments (62.9 mW × 5% = 3.1 mW), the internal signal power P_s was taken to be 1.3 mW which was estimated from the external signal power of 2.9 mW by considering the Fresnel reflection and mode coupling factor. It can be observed that the generated DF power increases as the sample length increases until it reaches the maximum value of 59 nW. Further increase in L gives rise to a reduction in the DF power due to the adverse effects of linear propagation losses. Also in Fig. 8, the impacts of TPA ($\alpha_{2,p(s,DF)}$), SPM ($n_{2,p(s,DF)}$), GVM ($GVM_{DF,p}$), and GVD ($GVD_{p(s,DF)}$) on the DF power were examined. From the figure, the existence of any of TPA, SPM, GVM, and GVD will reduce the generated DF power. The impact of SPM is small under the low power levels of the pump and signal, while TPA degrades the maximum power of DF by 25% because of the large TPA coefficient of the pump whose photon energy (E_p) is close to the bandgap of the waveguide core material (E_{gc}) ($E_p \approx 0.8E_{gc}$) and the relatively high peak power of the pump pulses. Moreover, GVD can degrade the maximum DF power by 2%, while GVM degrades it by about 1.1 orders of magnitude due to the pulse walk-off of the interacting harmonics. The final maximum DF power is about 4.3 nW at $L=2.5$ mm when considering all the effects of TPA, SPM, GVD, and GVM. As such, it is believed that, in the picosecond pulse regime, the major limiting factors in enhancing the DF power are TPA and GVM between the pump and DF signal.

Table 2. Simulation Parameters of BRW

Parameter	Value
Nonlinear interaction	Type II
d_{eff}	40.0 pm/V
$(\alpha_{0,DF},\alpha_{0,s},\alpha_{0,p})$	(2.0,2.2,5.0)/cm
$(\alpha_{2,DF},\alpha_{2,s},\alpha_{2,p})$	(0.03,0.15,11.5) cm/GW
$n_{2,DF}$	3.4×10^{-5} cm^2/GW
$n_{2,s}$	3.7×10^{-5} cm^2/GW
$n_{2,p}$	-1.2×10^{-5} cm^2/GW
$(A^{(3)}_{eff,DF},A^{(3)}_{eff,s},A^{(3)}_{eff,p})$	(6.7,6.6,3.2) μm^2
$GVM_{DF,p}$(pulsed,cw)	(−10.67,0) ps/mm
GVD_{DF}(pulsed,cw)	(5.65,0) $fs^2/\mu m$
GVD_s(pulsed,cw)	(5.65,0) $fs^2/\mu m$
GVD_p(pulsed,cw)	(170,0) $fs^2/\mu m$
Pulse width	2 ps
Pulse repetition rate	76 MHz

To better understand the effects of $\chi^{(3)}$ and mode dispersions on DFG, cw DFG was also simulated in which GVM and GVD can be ignored and the effects of TPA and SPM are significantly suppressed. As shown in Fig. 9, the length dependence of DF powers with and without considering the effects of TPA and SPM were plotted together. All the four curves are overlapped, which means that both the effects of TPA and SPM are neglectable under this low pump and signal power levels. The maximum DF power is about 89 nW at $L=5$ mm. For a special length $L=1.5$ mm used in the experiments, the DF power was read to be 34 nW, which is about nine times larger than that of pulsed DF power from simulation. This is consistent with the fact that cw DFG can give us more DF power observed in the experiments.

Figure 10(a) is the simulated DF power as a function of the average pump power for a sample with $L=1.5$ mm. The solid line is obtained from pulsed pumped DFG by in-

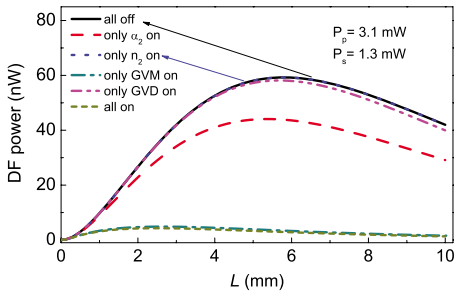

Fig. 8. (Color online) Simulated DF output power as a function of sample length, where the effects of TPA with coefficient α_2, SPM with coefficient n_2, GVM, and GVD are independently included. All curves were obtained with a 2 ps pulsed pump and a cw signal. P_p and P_s were set as 3.1 and 1.3 mW, respectively.

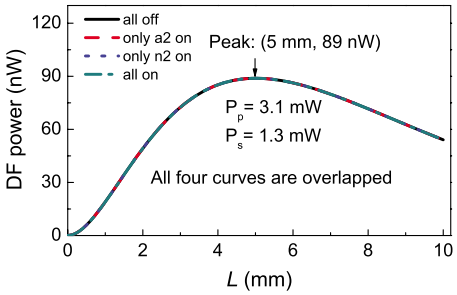

Fig. 9. (Color online) Simulated DF output power as a function of sample length, where the effects of TPA with coefficient α_2 and SPM with coefficient n_2 are independently included. All curves were obtained with cw pump and cw signal. P_p and P_s were set as 3.1 and 1.3 mW, respectively.

cluding the effects of SPM, TPA, GVM, and GVD, while the dashed line is the result obtained from cw pump with the effects of SPM and TPA. It can be seen that the DF powers increase with the increasing of pump power for both the pulsed- and cw-pumped processes, and the cw-pumped interaction can give us higher DF output under the same average pump powers. DF powers of 220 and 38 nW were obtained for pulsed-wave- and cw-pumped processes, respectively, with the average pump power of 20 mW. The lower output DF power of the pulsed pumped DFG was partially attributed to the short interaction time domain of the pulsed pump with the cw signal except the effects of TPA and GVM mentioned in the former part. Figure 10(b) is the corresponding conversion efficiency extracted from Fig. 10(a). The solid line is the data for pulsed pumped DFG, while the dashed line is that of the cw-pumped one. The conversion efficiency of the pulsed pumped DFG decreases from 0.20% W^{-1} to 0.14% W^{-1} as the pump power increases from 0 to 20 mW, while the value for the cw-pumped process remains around 0.84% W^{-1} during this entire power sweeping range. The reduction in the pulsed pump conversion efficiency is mainly due to the degrading effect of TPA.

5. DISCUSSION

The phase-matched DFG process is attractive since it can be used in optical parametric amplification [10] and optical parametric oscillation [26]. The attributes of PM using BRW waveguides come to light once its DFG performance is comparable with its counterparts which have already been used to build OPOs [26,27]. For the case of using the BRW structure as a chip with external pump, the main limitation in improving the generated DF power of the device is the low BRW mode coupling efficiency. Several routes can be undertaken to further enhance the DFG process in BRWs. These include preferential coupling to Bragg mode using prism coupling and grating-assisted coupling or using spatial light modulators for mode matching. In a more advanced scheme, these coupling techniques can be completely avoided by developing self-pump DFG devices, where a Bragg laser pump [28] with phase-matched cavity is fabricated on the same wafer platform.

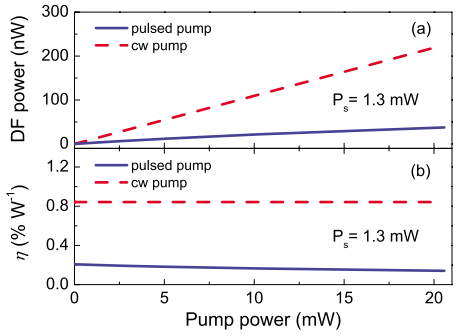

Fig. 10. (Color online) Simulated (a) DF power and (b) internal conversion efficiency η as functions of pump power for a sample with $L=1.5$ mm. The solid line represents pulsed pumped DFG which includes the effects of SPM, TPA, GVM, and GVD with their numerical values summarized in Table 2; while the dashed line is the cw-pumped DFG which was obtained by including the effects of SPM and TPA.

As discussed in Section 4, the effects of $\chi^{(3)}$ on cw DFG can be neglected under low average powers. From Fig. 9, the optimum length of the device is $L=5$ mm. The DF power of 14 μW can be obtained for a given internal pump power of 500 mW and signal power of 1.3 mW in this case, and the corresponding conversion efficiency is about 2.2% W^{-1}. The degrading effect of $\chi^{(3)}$ is under 1%. Further increase in the pump or signal power can give us more output DF power, for example, the DF power of 1.1 mW can be obtained if we increase the signal power to 100 mW. So, the limitation of cw DFG is linear losses of the harmonics which is related to the fabrication processes of the device.

For pulsed DFG, TPA and GVM are the two main limitations in increasing the DFG efficiency. For a device with $L=1.5$ mm, the DF power is only about 204 nW with the internal pump and signal powers of 500 and 1.3 mW, respectively. The corresponding conversion efficiency is about 0.03% W^{-1}, which is about 70 times smaller than that of cw DFG. The TPA and GVM degrade the DF efficiency by 3.5 and 2.3 orders of magnitudes, respectively, when they solely exist. The effect of TPA can be suppressed by shifting the pump wavelength to a longer one at which TPA coefficient is much smaller, while GVM can be reduced by optimizing the device structure. The conversion efficiency is believed to be significantly higher if the peak power of the signal laser can be increased or the pulsed signal source can be used in phase during the interaction. Reducing the propagation losses will also increase the generated powers for all modes of operation; this can be achieved by optimizing the fabrication processes.

6. CONCLUSIONS

Pulsed- and continuous-wave (cw) type-I and type-II DFG processes were characterized in AlGaAs BRWs. The PM bandwidth of exceeding 40 nm was observed in all the processes. The highest DF power of 2.45 nW was obtained in the cw type-II interaction with the external average pump and signal powers of 62.9 and 2.9 mW, respectively. The conversion efficiency is about 1.3×10^{-3}% W^{-1} for a sample with a length of 1.5 mm, which corresponds to the normalized conversion efficiency of 5.8×10^{-2}% W^{-1} cm^{-2}. Using the split-step Fourier method, the impact of third-order nonlinearities including TPA and SPM on the effi-

ciency of the DFG was numerically investigated. Furthermore, the adverse effects of GVM and GVD of the interacting waves on the efficiency of pulsed DFG were studied using the same method. Theoretical simulations indicated that TPA and GVM between pump and DF signal were the main limitations in enhancing the DF power, hence limiting the efficiency of the pulsed nonlinear interaction.

ACKNOWLEDGMENTS

The authors are thankful to J. S. Aitchison for making the Ti:Sapphire laser available and to the Natural Sciences and Engineering Research Council of Canada.

REFERENCES

1. D. Rehle, D. Leleux, M. Erdelyi, F. Tittel, M. Fraser, and S. Friedfeld, "Ambient formaldehyde detection with a laser spectrometer based on difference-frequency generation in PPLN," Appl. Phys. B **72**, 947–952 (2001).
2. U. Willer, M. Saraji, A. Khorsandi, P. Geiser, and W. Schade, "Near- and mid-infrared laser monitoring of industrial processes, environment and security applications," Opt. Lasers Eng. **44**, 699–710 (2006).
3. S. Woutersen, U. Emmerichs, and H. J. Bakker, "Femtosecond mid-IR pump-probe spectroscopy of liquid water: evidence for a two-component structure," Science **278**, 658–660 (1997).
4. C. J. Wang and P. Sahay, "Breath analysis using laser spectroscopic techniques: Breath biomarkers, spectral fingerprints, and detection limits," Sensors **9**, 8230–8262 (2009).
5. J. M. Schmitt, "Optical coherence tomography (OCT): a review," IEEE J. Sel. Top. Quantum Electron. **5**, 1205–1215 (1999).
6. P. Bravetti, A. Fiore, V. Berger, E. Rosencher, J. Nagle, and O. Gauthier- Lafaye, "5.2–5.6-μm source tunable by frequency conversion in a GaAs-based waveguide," Opt. Lett. **23**, 331–333 (1998).
7. D. Zheng, L. A. Gordon, Y. S. Wu, R. S. Feigelson, M. M. Fejer, and R. L. Byer, "16-μm infrared generation by difference-frequency mixing in diffusion-bonded stacked GaAs," Opt. Lett. **23**, 1010–1012 (1998).
8. K. L. Vodopyanov, "Optical THz-wave generation with periodically-inverted GaAs," Laser Photonics Rev. **2**, 11–25 (2008).
9. M. H. Dunn and M. Ebrahimzadeh, "Parametric generation of tunable light from continuous-wave to femtosecond pulses," Science **286**, 1513–1517 (1999).
10. E. Guillotel, M. Ravaro, F. Ghiglieno, C. Langlois, C. Ricolleau, S. Ducci, I. Favero, and G. Leo, "Parametric amplification in GaAs/AlO_x waveguide," Appl. Phys. Lett. **94**, 171110 (2009).
11. A. Fiore, V. Berger, E. Rosencher, P. Bravetti, N. Laurent, and J. Nagle, "Phase-matched mid-infrared difference frequency generation in GaAs-based waveguides," Appl. Phys. Lett. **71**, 3622–3624 (1997).
12. S. J. B. Yoo, C. Caneau, R. Bhat, M. A. Koza, A. Rajhel, and Neo Anoniades, "Wavelength conversion by difference frequency generation in AlGaAs waveguides with periodic domain inversion achieved by wafer bonding," Appl. Phys. Lett. **68**, 2609–2611 (1996).
13. D. S. Hum and M. M. Fejer, "Recent advances in crystal optics," C. R. Phys. **8**, 180–198 (2007).
14. A. S. Helmy, "Phase matching using Bragg reflection waveguides for monolithic nonlinear optics applications," Opt. Express **14**, 1243–1252 (2006).
15. A. S. Helmy, B. Bijlani, and P. Abolghasem, "Phase matching in monolithic Bragg reflection waveguide," Opt. Lett. **32**, 2399–2401 (2007).
16. S. J. Wagner, A. A. Muhairi, J. S. Aitchison, and A. S. Helmy, "Modeling and optimization of quasi-phase matching via domain-disordering," IEEE J. Quantum Electron. **44**, 424–429 (2008).
17. J. B. Han, P. Abolghasem, B. J. Bijlani, A. Arjmand, S. Chaitanya Kumar, A. Esteban-Martin, M. Ebrahim-Zadeh, and A. S. Helmy, "Femtosecond second-harmonic generation in AlGaAs Bragg reflection waveguides: theory and experiment," J. Opt. Soc. Am. B **27**, 1291–1298 (2010).
18. P. Abolghasem, J. Han, A. Arjmand, B. J. Bijlani, and A. S. Helmy, "Highly efficient second-Harmonic generation in monolithic matching-layer enhanced $Al_xGa_{1-x}As$ Bragg reflection waveguides," IEEE Photon. Technol. Lett. **21**, 1462–1464 (2009).
19. J. B. Han, P. Abolghasem, D. Kang, B. J. Bijlani, and A. S. Helmy, "Difference-frequency generation in AlGaAs Bragg reflection waveguides," Opt. Lett. **35**, 2334–2336 (2010).
20. R. A. Baumgartner and R. L. Byer, "Optical parametric amplification," IEEE J. Quantum Electron. **15**, 432–444 (1979).
21. G. P. Agrawal, *Nonlinear Fiber Optics*, 2nd ed. (Academic, 1995).
22. J. S. Aitchison, D. C. Hutchings, J. U. Kang, G. I. Stegeman, and A. Villeneuve, "The nonlinear optical properties of AlGaAs at the half band gap," IEEE J. Quantum Electron. **33**, 341–348 (1997).
23. E. W. Van Stryland, M. A. Woodall, H. Vanherzeele, and M. J. Soileau, "Energy band-gap dependence of two-photon absorption," Opt. Lett. **10**, 490–492 (1985).
24. B. S. Wherrett, "Scaling rules for multiphoton interband absorption in semiconductors," J. Opt. Soc. Am. B **1**, 67–72 (1984).
25. M. Sheik-Bahae, D. C. Hutchings, D. J. Hagan, and E. W. Van Stryland, "Dispersion of bound electron nonlinear refraction in solids," Opt. Quantum Electron. **27**, 1296–1309 (1991).
26. K. L. Vodopyanov, O. Levi, P. S. Kuo, T. J. Pinguet, J. S. Harris, M. M. Fejer, B. Gerard, L. Becouarn, and E. Lallier, "Optical parametric oscillation in quasi-phase-matched GaAs," Opt. Lett. **29**, 1912–1914 (2004).
27. P. S. Kuo, K. L. Vodopyanov, M. M. Fejer, X. Yu, J. S. Harris, D. F. Bliss, and D. Weyburne, "GaAs optical parametric oscillator with circularly polarized and depolarized pump," Opt. Lett. **32**, 2735–2737 (2007).
28. B. J. Bijlani and A. S. Helmy, "Bragg reflection waveguide diode lasers," Opt. Lett. **34**, 3734–3736 (2009).